Line vortices and the vacillation of Langmuir circulation

Malarkey, J.; Thorpe, Stephen

Journal of Physical Oceanography

DOI:
10.1175/JPO-D-16-0006.1

Published: 23/06/2016

Publisher's PDF, also known as Version of record

Line Vortices and the Vacillation of Langmuir Circulation

J. MALARKEY AND S. A. THORPE

School of Ocean Sciences, Bangor University, Menai Bridge, Anglesey, United Kingdom

(Manuscript received 17 November 2015, in final form 11 April 2016)

ABSTRACT

Three types of breakdown of Langmuir circulation (Lc) are observed, two of which are represented in large-eddy simulation (LES) models, but the third, vacillation, is not. The stability of Lc can be examined by representing the downwind-aligned vortices by line vortices that are subjected to perturbations. Earlier conclusions relating to stability in homogeneous water of infinite depth are found to be in error because no stationary unperturbed state exists. The motion of vortices is examined and shown to be consistent with an explanation of Lc devised by Csanady. Motion of line vortices in water of limited depth or bounded below by a thermocline is examined. The motion replicates some of the features of vacillation observed by Smith in deep water bounded by a thermocline, including its periodicity and fluctuations in the formation of bubble bands. Vortices describe closed orbits within the Langmuir cells. Particle motions in the vacillating Lc pattern exhibit trapping close to the line vortices or near the cell boundaries. Vacillation appears not to have been observed in water of limited depth. Here, the vacillation period is predicted to be longer than the deep-water equivalent and may be too long for vacillations to be detected.

1. Introduction

Langmuir circulation (Lc) is reviewed by Leibovich (1983), Pollard (1977), and Thorpe (2004). It is now recognized as a major contributor to turbulence and dispersion in the upper layers of lakes, coastal seas, and the ocean. Instability of the flow driven by wind and waves beneath a water surface results in the formation of a regular array of counterrotating vortices within "Langmuir cells" with axes directed downwind. Following earlier analysis by Thorpe (1992) and Csanady (1994) the vortices are represented here by line vortices. These lead to lines of convergence on the sea surface, producing the commonly observed rows of flotsam or windrows, aligned in the wind direction and first studied by Langmuir (1938). Convergence also leads to the accumulation of subsurface bubbles produced by breaking surface waves. The resulting "bubble bands" can be detected acoustically (Thorpe and Hall 1983; Farmer and Li 1995; Smith 1998; Gemmrich and Farmer 1999).

The stable circulation tends to constrain the "transverse" dispersion of floating particles or chemical films in a direction normal to the wind; buoyant particles or oil accumulates in the windrows. Transverse dispersion at scales exceeding the distance between windrows occurs when Langmuir cells break down as a consequence of the instability of the Lc pattern (Thorpe et al. 1994; Thorpe 2009); dispersion is largely controlled by the instability, the main topic of this paper. We draw attention to the present lack of observational information regarding the instability of Langmuir cells and propose a novel explanation for their vacillation, as observed by Smith (1998).

The paper is arranged as follows: Observations of the spatial irregularity of Langmuir cells are described in section 2. Three types of irregularity are found. Analytical and numerical models of Lc are described in section 3, and the results are compared with observations. The use of line vortex models is briefly reviewed in section 4. An error in the earlier results for the stability of Lc in a homogeneous ocean of infinite depth by Thorpe is reported in section 5. A study is made of how vortices move. This relates to Csanady's (1994) proposal for the generation of Lc. Section 6 describes results in

Denotes Open Access content.

Corresponding author address: J. Malarkey, School of Ocean Sciences, Bangor University, Menai Bridge, Anglesey, LL59 5AB, United Kingdom.
E-mail: j.malarkey@bangor.ac.uk

DOI: 10.1175/JPO-D-16-0006.1

which motion is constrained by finite depth or an underlying thermocline, collectively referred to as "finite-depth" fluids. A general solution is first presented (section 6a) before the effect of a small-amplitude perturbation is examined (one that leads to the motion of vortices in closed orbits; section 6b), followed by the effect of a finite perturbation (section 6c). The latter includes the study of vortices that are unequally spaced and of the oscillatory motion or vacillations that develop. The main conclusions are presented and discussed in section 7.

2. Photographic and acoustic observations of the stability of Langmuir bands

Still photographs of the distribution of material floating on the sea or a lake surface provide some limited information about the continuity of windrows and hence of Lc. The buoyant material may consist of algae or floating bubbles (i.e., foam) generated by breaking waves (e.g., Thorpe 2004), oil following its accidental or deliberate release (e.g., Faller 1971; Thorpe 2004, seen in an infrared image in his Fig. 5), or computer cards scattered to make convergence bands visible (e.g., Weller and Price 1988). Several photographs showing extensive areas of a water surface and numerous windrows have been published. Stommel (1951) shows aerial images of the signature parallel streaks [reproduced by Faller and Auer (1988) in the Great Salt Lake and on the Banana River, Florida]. Kenney (1977) has several photographs of foam bands in the Lake of the Woods (49°01′N, 94°30′W). Bands are generally continuous for distances of typically 8 times their separation before merging with neighboring bands or losing their identity. This may, however, represent an overestimate of the mean length of Langmuir cells because of a tendency to select photographs that emphasize the regularity and extent of the windrows and therefore contain bias to longer floating bands. Furthermore the existence of a band does not necessarily imply the presence of active convergent motion; it may be a "fossil" remaining from previous motion. More photographs, particularly time-lapse images recording the time history of windrows, would be useful in establishing the scale and mechanism of band disruption. Three apparently distinct types of breakdown of the linear pattern of parallel windrows or bubble clouds have been observed acoustically.

a. *Interruptions to bands*

The first is simply interruptions in the continuity of bands. Although there are numerous sonograph images of the bubble bands as they drift through a single, fixed, side-scan sonar beam pointing across the wind direction (e.g., Thorpe 1992), so producing a range versus time record of the bands, these contain no information in the along-band direction and therefore do not resolve or identify the nature of the spatial instability of the bands unambiguously. Images of bubble clouds obtained by a 100-kHz 360° scanning sonar with a range of about 300 m deployed by Gemmrich and Farmer (1999) west of Monterey Bay, California, and drifting with the mean flow are more useful. These show the spatial distribution of near-surface bubble bands, typically extending down to a depth of 1–4 m (Zedel and Farmer 1991). An image reproduced as Fig. 4 in Gemmrich and Farmer (1999; see also Fig. 4 in Thorpe 2004) show that the length L_0 of the bands is typically about 260 m before bifurcating or being interrupted by a band with a different orientation, and their separation s is about 50 m: $L_0/s \approx 5.2$. The larger bands persist for up to 25 min as they are advected by the mean flow. Rather than being continuous, they are composed of linear patches of bubbles typically of length $L_1 \sim 100$ m: $L_1/s \approx 2.0$. While the patchy nature of the bands may indicate the instability of Lc, it is impossible to tell unequivocally whether this is so. Gaps in a band of bubbles may be a consequence of the local absence of convergence (since without the downward motion located beneath the lines of convergent flow, bubbles will rise to the surface and the bands will disappear). The supply of bubbles into the surface convergence zones is, however, itself intermittent, coming from the spatially and temporally variable injection from breaking waves or wave groups and leading to a variable concentration of bubbles in the convergence bands.

b. *Y junctions*

Amalgamation of two neighboring rows at an angle of about 30° in downwind-pointing "Y junctions" is observed by Farmer and Li (1995) in the Strait of Georgia, using a 100-kHz 90° sector-scanning sonar system with a range of about 270 m. Bubble bands are typically 60 m long, about 3 times their spacing, before combining together. The instability leading to the junction of bands is ascribed to that described by Thorpe (1992) in a study of the instability of vortex lines (see sections 5, 6a, and 6b) and is illustrated schematically by Farmer and Li as being similar to the vortex connection described by Crow (1970) for a parallel vortex pair.

c. *Vacillations*

Finally, "vacillation" is reported by Smith (1998, his sections 4.3 and 5.3) using measurements from a 195-kHz phase-locked acoustic Doppler sonar (PADS) some 100 km off Point Arguello, California. This system operates with a beam-formed system to produce images of the motion of bubble clouds in a 25°-wide sector lying

horizontally across the sea surface with a range from 190 to 450 m. Because the mean volume of bubbles decays rapidly with depth, their scattering cross section decaying exponentially over distances of about 1 m, the dominant sampling depths are typically 1 to 2 m below the wave troughs. Smith observes downwind-aligned bands of bubbles with a mean separation of about 50 m, roughly twice the depth of the mixed layer, so that the Langmuir cells are approximately square. [These contrast with the size of Langmuir supercells observed by Gargett and Wells (2007), which in a water depth of about 15 m reach the seabed and have a width of 3–6 times their vertical scale.] The extent of the area covered by the sonar is insufficient to judge the length L_0 of bands with confidence; comparison of L_0/s with Gemmrich and Farmer's observations is not possible but L_1/s is about 2, in accord with Gemmrich and Farmer. Root-mean-square (rms) velocity fluctuations are about 3.5 cm s^{-1}. Vacillation occurs during a spell of relatively constant winds of about 15 m s^{-1} and of steady direction, until terminated apparently by a reduction in wind speed and a change in its direction. Vacillation is characterized by variations between relatively disorganized weaker flows, where the acoustic reflections from bands are relatively small and consequently the bands themselves are poorly defined, and more intense and regular-banded features. Four such vacillations are observed with a mean period of about 30 min. Variations are also seen in the rms surface velocity of amplitude of about 0.25 cm s^{-1}, out of phase with the strength of acoustic scattering, so that the maximum scattering intensity corresponds to the rms velocity minimum. The maximum speed of the converging motion toward windrows in this period is about 0.2 m s^{-1} (J. A. Smith 2015, personal communication). There are also accompanying changes in the spacing of bands of order 4 m (i.e., ~8%), with slightly smaller scales coinciding with strong scattering, low velocity levels, and vice versa, but no changes in the orientation of the bands. The observed vacillation is not correlated with changes in mixed layer depth (e.g., caused by internal waves), changes in wind speed and direction, or the magnitude of vertical straining by the flow field. No other reports of vacillation appear to be available, perhaps because of the lack of observations at relatively high wind speeds.

3. Analytical and LES models of Langmuir circulation and its breakdown

a. *Analytical models based on Craik and Leibovich*

Much theoretical study of Lc is made using equations devised by Craik and Leibovich (e.g., the CL2 model; Craik and Leibovich 1976) including the "vortex force" and Stokes drift. The dimensional quantities governing the flow are the friction velocity u_* on the water side of the sea surface, the magnitude of the Stokes drift U_{S0} at the surface, the eddy viscosity ν_T, and vertical e-folding decay length scale β^{-1} of the Stokes drift. One objective of research has been to identify the bifurcations or instabilities that occur as parameters such as the inverse Langmuir number

$$\mathrm{La}^{-1} = (U_{S0}/u_*)^{1/2}(u_*/\nu_T\beta)^{3/2}, \tag{1}$$

describing the strength of the forcing change (e.g., Li and Garrett 1993). The primary instability as La^{-1} increases beyond a critical value La_c^{-1} is the set of counterrotating vortices resembling the observed cell structure of Lc. Further increase in La^{-1} leads to vacillating waves and "traveling defects" (Tandon and Leibovich 1995). The term vacillation is taken from that used in a similar analysis applied to thermal convection by Clever and Busse (1992). The vacillating motion described by Tandon and Leibovich alternates between a highly distorted roll state and a nearly two-dimensional roll state but with a periodicity of tens of hours and is therefore discounted by Smith as an explanation for his observed 30-min vacillation. Smith is unable to reconcile observations and the stability theory of Tandon and Leibovich (1995). His suggestion that buoyancy forcing by bubbles may lead to the observed vacillation is refuted by Farmer et al. (2001).

By comparing Eulerian and Lagrangian fields, Bhaskaran and Leibovich (2002) devise a model for downwind-pointing Y junctions but do not make a prediction of their periodicity.

b. *LES models*

Recognition of its variability and contribution to turbulence in the upper-ocean mixed layer has led to the study of "Langmuir turbulence" using large-eddy simulation (LES) models (see, e.g., Skyllingstad and Denbo 1995; McWilliams et al. 1997; Noh et al. 2004; Sullivan et al. 2007; Noh et al. 2011; McWilliams et al. 2012). These studies provide some guidance to the possible nature of the breakdown of regular Langmuir cells. Rather than using the parameter La depending on an assumed constant ν_T (in reality a function of the turbulence and variable in depth), the turbulent Langmuir number

$$\mathrm{La}_t = (u_*/U_{S0})^{1/2} \tag{2}$$

is generally adopted to characterize the flow, plus a Reynolds number, and (if the buoyancy flux through the water surface

is nonzero) the Hoenikker number. Oceanic values of La_t when Lc is observed are typically about 0.3. Favorable comparisons with observations are found only in LES models that account for the processes (e.g., Stokes drift) through which Lc is forced. Compared features include (i) the development of the linear downwind structure characteristic of Lc [McWilliams et al. (1997, their Fig. 12) and Kukulka et al. (2010, see their Fig. 9); both figures compare Langmuir turbulence with shear turbulence], (ii) the evolution of crosswind velocity variance and mixed layer deepening (Kukulka et al. 2010), and (iii) the ratio of crosswind velocity variance to the friction velocity (Li et al. 2005). The construction of regime diagrams by Li et al. (2005) and Belcher et al. [2012; although challenged by Sutherland and Melville (2015)] have provided a basis for understanding and demonstrating the importance of Lc in driving ocean turbulence.

The downward vertical velocity w at a fixed depth near the surface serves as a useful surrogate for the convergence, and its banded structure is shown by several authors. Like the bubble bands detected acoustically, the structure of convergence bands is patchy. We characterize the structures by estimates of the typical band separations s, lengths L_0, and patch lengths L_1 (all in meters) at given values of La_t, specifying values of R, where $R = (s, L_0, L_1; La_t)$. From Skyllingstad and Denbo (1995, their Fig. 5), we find $R = (25, 70, 40; 0.26)$ when forcing is by wind stress and vortex force only. McWilliams et al. (1997, their Fig. 12) has $R = (17, 120, 30; 0.3)$; they remark that the patterns of bands are about as well organized as those observed and find many examples of Y junctions in the models' near-surface flow field. Skyllingstad et al. (1999, their Fig. 5a) has $R = (20, 130, 30; 0.3)$, Noh et al. (2004, their Figs. 1 b and d) have $R = (50, 180, 50; 0.45)$, and Y junctions are observed, while Kukulka et al. (2010, their Fig. 9) have $R = (35, 200, 70; 0.3–0.6)$. Values of L_0/s range from 2.8 to 7.1 with an average of 5.2 ± 1.7 (plus or minus one standard deviation), the mean coinciding (probably coincidently) with that found in Gemmrich and Farmer's (1999) observations described in section 2a. The average value of L_1/s is 1.6 ± 0.4, smaller than Gemmrich and Farmer's 2.0. The length of bands of particles advected by the flow modeled by Skyllingstad and Denbo (1995, their Fig. 8) are generally longer than the length over which the vertical velocity w remains coherent so that L_1 may be underestimated from the bands of high w in the model.

Although LES models demonstrate the first two types of the observed breakdown of linear bands (sections 2a and 2b), there is no clear evidence of vacillation (section 2c).

4. Line vortex models

For over a hundred years line vortices have proved useful in understanding and predicting the development of flows and instabilities that occur in transitions from laminar flows to turbulence. The stability of two-dimensional perturbations to the wake in the lee of a cylinder, composed of two lines of vortices of opposite signs and now known as a Kármán vortex street, is studied by von Kármán (1911, 1912) and is described by Lamb (1932, section 156). Rosenhead (1929) examines the effects of adding plane boundaries. The three-dimensional instability of a pair of vortices of opposite sign, Crow instability, is described using line vortices but with finite cores (Crow 1970). Multivortex models are used to describe flow separation over steep, two-dimensional sand ripples (Longuet-Higgins 1981; Malarkey and Davies 2002). Vortex generation by deep-water breakers is discussed by Pizzo and Melville (2013), referring to Csanady's (1994) description of how a pair of horizontal vortices of opposite signs produced by a breaking wave interact with each other and with their images in the sea surface; the vortices approach one another and move downward from the sea surface. Both two- and three-dimensional instability of vortex arrays are studied by Robinson and Saffman (1982). Their methodology is used by Deloncle et al. (2011) to investigate the onset of zigzag instability and by Thorpe (1992) to investigate the stability of Lc.

In Thorpe's vortex model the circulation pattern in an array of Langmuir cells is represented by a horizontal set of parallel equally spaced (separation l) line vortices of equal circulation Γ but of signs alternating in the horizontal x direction. The vortices located at horizontal positions $x = (m + \frac{1}{2})l$ have circulations $(-1)^{m+1}\Gamma$, where m is an integer ranging from $-\infty$ to ∞ and positive circulations are clockwise. The cell boundaries where the horizontal velocity is zero are at horizontal positions $x = ml$ (two cell widths or the spacing between like-signed vortices are equivalent to the separation of bubble bands referred to in sections 2 and 3; $s = 2l$). It is implicit in this representation that the processes forcing the Lc are no longer active or, at least, that the forcing is significantly less than that of any process that leads to the perturbation of the cell pattern. Thorpe considers two cases in which the vortex lines are perturbed from given initial states. The small perturbation stability analysis assumes that the initial state is static or at least steady with the whole array moving at a uniform speed [e.g., as in the analysis of the stability of a symmetrical double row of vortices described by Lamb (1932, section 156)].

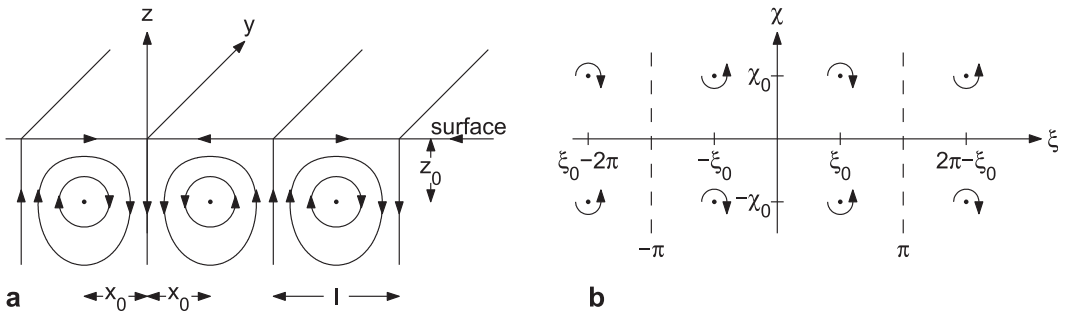

FIG. 1. Definition sketches of infinite-depth Langmuir circulation for equal spacing (a) dimensional and (b) nondimensional in the complex ζ plane. The notation, using x_0 and ξ_0, anticipates unequal spacing (equal horizontal spacing is given by $x_0 = l/2$ and $\xi_0 = \pi/2$).

5. A vortex model of Langmuir cells in infinite depth

In Thorpe's first case, the vortices are at a level, $z = -z_0$, below a horizontal surface at $z = 0$ in homogenous water of infinite depth, as shown in Fig. 1a. We examine in this section how vortices will move, applying results to earlier studies of Thorpe and Csanady.

The vertical motion at the surface is constrained to be zero by a set of image vortices with circulations of $(-1)^m\Gamma$ at the same horizontal positions $x = (m + \frac{1}{2})l$ but at a level of $z = z_0$. In anticipation of the fact that the vortices may not be equally spaced in the horizontal, the real and image arrays of vortices can each be subdivided into arrays of like-signed circulations: two arrays of real vortices, $-\Gamma$ at $(2ml + x_0, -z_0)$ and Γ at $(2ml - x_0, -z_0)$, and two of image vortices, Γ at $(2ml + x_0, z_0)$ and $-\Gamma$ at $(2ml - x_0, z_0)$, where x_0 is the horizontal distance of the vortex to the nearest point of convergence at the edge of the cell (see Fig. 1a). Thorpe's equal spacing then corresponds to the special case where $x_0 = l/2$. Regardless of the value of x_0, the cell boundaries remain fixed at $x = ml$. To facilitate the analysis, the coordinate system can be nondimensionalized by the horizontal spacing wavenumber $2\pi/2l = \pi/l$ (where $2l$ corresponds to the spacing between like signed vortices). Thus, if $\xi = \pi x/l$, $\chi = \pi z/l$, then Lc can be represented in the cross section in the complex ζ plane, where $\zeta = \xi + i\chi$ and $i = (-1)^{1/2}$ as shown in Fig. 1b. The configuration comprises four infinite arrays of vortices each with spacing of 2π located at $\zeta = -\zeta_0 + 2m\pi$, $\zeta_0^* + 2m\pi$, $-\zeta_0^* + 2m\pi$, and $\zeta_0 + 2m\pi$, with circulations Γ, $-\Gamma$, $-\Gamma$, and Γ, respectively, where $\zeta_0 = \xi_0 + i\chi_0$, $\xi_0 = \pi x_0/l$, $\chi_0 = \pi z_0/l$, and the * represents the complex conjugate ($\xi_0 = \pi/2$ for equal spacing).

In the complex ζ plane, an isolated line vortex at $\zeta = \zeta_0$ with a circulation Γ has a complex potential given by $\Omega = i(\Gamma/2\pi)\log(\zeta - \zeta_0)$; when $\zeta \neq \zeta_0$, the horizontal and vertical velocity u and w are given by $u - iw = (\pi/l)d\Omega/d\zeta$, which is

$$u - iw = \frac{iU}{\zeta - \zeta_0}, \tag{3}$$

where U is a characteristic velocity ($=\Gamma/2l$). The velocity of a vortex at $\zeta = \zeta_0$ is calculated by removing the self-potential before the derivative of Ω is calculated (Milne-Thomson 1962, section 13.22). In the case of an isolated vortex, the self-potential is Ω so the vortex velocity is zero, but this will not always be the case for multiple vortices. If the vortices are being perturbed from their regularly spaced positions, the effect of all the other vortices on the vortex located at $\zeta = \zeta_0$ can be determined by summing up the contributions using Eq. (3). However, if vortices are unperturbed and their array spacing is being maintained, advantage can be taken of the expression for the complex potential of an infinite array of equally spaced vortices (Lamb 1932, section 156) such that for line vortices located at $\zeta_0 + 2m\pi$:

$$\sum_{m=-\infty}^{\infty} i\frac{\Gamma}{2\pi}\log[\zeta - (\zeta_0 + 2m\pi)] = i\frac{\Gamma}{2\pi}\log\left[\sin\tfrac{1}{2}(\zeta - \zeta_0)\right]. \tag{4}$$

Treating the vortices as infinite arrays aids the analysis of regularly spaced modes since behavior of the four central vortices in each array at $\zeta = -\zeta_0$, ζ_0^*, $-\zeta_0^*$, and ζ_0 then represents all the vortices. The complex potential for this configuration of vortices is then simply

$$\Omega = i\frac{\Gamma}{2\pi}\log\left[\frac{\sin\tfrac{1}{2}(\zeta + \zeta_0)}{\sin\tfrac{1}{2}(\zeta - \zeta_0^*)}\right] + i\frac{\Gamma}{2\pi}\log\left[\frac{\sin\tfrac{1}{2}(\zeta - \zeta_0)}{\sin\tfrac{1}{2}(\zeta + \zeta_0^*)}\right], \tag{5}$$

where the first and second terms are the complex potentials of all the vortices at $-i\chi_0$ and their images at $i\chi_0$, respectively. The velocity is

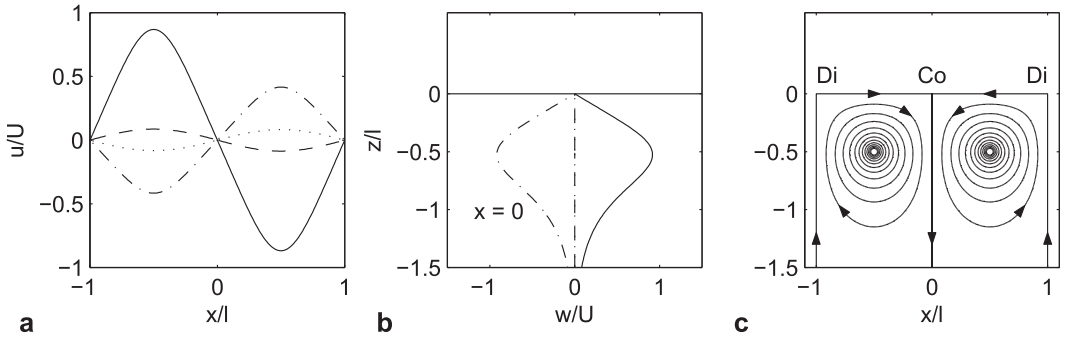

FIG. 2. Shows (a) u at $z = 0$ (solid), $-l/2$ (dashed), $-l$ (dashed–dotted), and $-3l/2$ (dotted), (b) w at $x = -l$ (solid), $-x_0$ (dashed), 0 (dashed–dotted), and x_0 (dotted), where w at $x = \pm x_0$ lie on top of one another, and (c) the streamlines for infinite-depth Lc for a vortex centered at $(x_0, -l/2)$, where $x_0 = l/2$, determined from Eqs. (6) and (5) with $\xi_0 = \pi/2$ and $\chi_0 = \pi/2$ (Co indicates convergence and Di indicates divergence).

$$u - iw = \frac{1}{2}U \times \begin{cases} i\cot\tfrac{1}{2}(\zeta + \zeta_0) - i\cot\tfrac{1}{2}(\zeta - \zeta_0^*) + i\cot\tfrac{1}{2}(\zeta - \zeta_0) - i\cot\tfrac{1}{2}(\zeta + \zeta_0^*), & \zeta \neq \zeta_0^*, -\zeta_0, \\ i\cot\xi_0 - \coth\chi_0 - i\cot\zeta_0^*, & \zeta = \zeta_0^*, \\ i\cot\xi_0 + \coth\chi_0 - i\cot\zeta_0, & \zeta = -\zeta_0, \end{cases} \tag{6}$$

where $U = \Gamma/2l$. Here, in the calculation of u–iw at $\zeta = \zeta_0^*$ and $-\zeta_0$, corresponding to the advection velocity of the vortices, the self-potential has first been removed as explained above. Figure 2 shows the horizontal and vertical velocity and streamlines based on contours of the streamfunction ψ [=Im(Ω), where Im is the imaginary part] determined from Eqs. (6) and (5) with $\xi_0 = \pi/2$ and $\chi_0 = \pi/2$, that is, for vortices at a depth $l/2$, which are equally spaced by a distance l in the horizontal. Evaluating Eq. (6) at the water surface, $\zeta = \xi$ with $\xi_0 = \pi/2$, results in a horizontal velocity given by

$$u(\xi) = -\frac{2U\sinh\chi_0\sin\xi}{\cosh^2\chi_0 - \sin^2\xi}, \tag{7}$$

so that $u(\pm\pi/2) = \mp 2U/\sinh\chi_0$, and there are surface convergences at $\xi = 2m\pi$ and divergences at $\xi = (2m + 1)\pi$, where m is any integer (see Fig. 2). From Eq. (6) it is evident that the vortices located at $\zeta = \zeta_0^*$ and $-\zeta_0$ are not stationary. When $\xi_0 = \pi/2$, the vortices have horizontal velocities given by

$$u(\pm\pi/2 - i\chi_0) = \mp\frac{1}{2}U(\coth\chi_0 - \tanh\chi_0) = \mp\frac{U}{\sinh 2\chi_0}, \tag{8}$$

so the two vortices shown in Fig. 2c move toward one another. An equally spaced row of vortices cannot induce a velocity in itself; thus, the horizontal component of velocity given by Eq. (8) is the result of the image vortices only. The assumption that the state illustrated in Fig. 1 is static with stationary vortices is therefore incorrect, and the basis of Thorpe's stability analysis is in error.

For vortices that are not equally spaced, $\xi_0 \neq \pi/2$, the velocity at the water surface, $\zeta = \xi$, from Eq. (6) is

$$u(\xi) = -\frac{2U\sinh\chi_0\sin\xi\sin\xi_0}{\cosh^2\chi_0 - 2\cosh\chi_0\cos\xi\cos\xi_0 + \cos^2\xi_0 - \sin^2\xi}, \tag{9}$$

so that $u(\pm\xi_0) = \mp 2U\sinh\chi_0\sin^2\xi_0/(\cosh^2\chi_0 - 2\cosh\chi_0\cos^2\xi_0 + \cos 2\xi_0)$. When $\xi_0 = \pi/2$, Eq. (9) simplifies to Eq. (7). Figure 3 shows the horizontal and vertical velocity and streamlines for the case where the vortex is centered at $(0.37l, -l/2)$, $\xi_0 = 0.37\pi$, and $\chi_0 = \pi/2$. It can be seen that surface convergences at $x = 2ml$ and divergences at $x = (2m + 1)l$ are maintained (this will in general be the case even though the vortices are moving). The vertical velocities at $x = -l$ and 0 are no long mirror images of one another; the vertical velocity associated with the convergence at $x = 0$ is far stronger because the vortex is closer to it.

In this infinite-depth case when the vortices are not equally spaced ($\xi_0 \neq \pi/2$), the initial vortex velocity will not be horizontal (see dotted line in Fig. 3b) and the vortices will trace out a curved path. The path that a vortex, initially located at $\zeta = \zeta_0^*$, follows can be determined from the vortex streamfunction $\psi(\zeta_0^*)$; $\psi(\zeta_0^*) = \mathrm{Im}[\Omega(\zeta_0^*)]$, where $\Omega(\zeta_0^*)$ is given by Eq. (5) evaluated at ζ_0^* with the self-potential removed $\Omega(\zeta_0{}^*) = i(\Gamma/2\pi)\log(-i\sinh\chi_0\sin\xi_0/\sin\zeta_0{}^*)$. The term $\psi(\zeta_0{}^*)$ is then

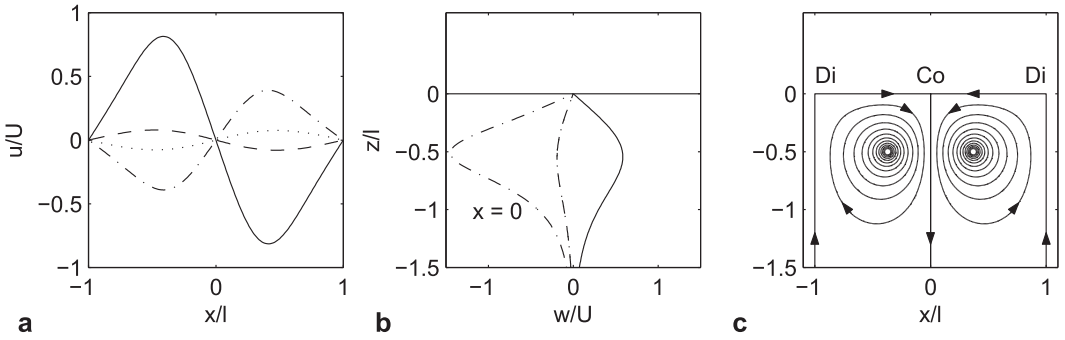

FIG. 3. As in Fig. 2, but where $x_0 = 0.37l$, determined from Eqs. (6) and (5) with $\xi_0 = 0.37\pi$ and $\chi_0 = \pi/2$.

$$\psi(\xi_0^*) = -\frac{\Gamma}{4\pi}\log(\cot^2\xi_0 + \coth^2\chi_0). \qquad (10)$$

Streamlines associated with Eq. (10) correspond to the path followed by a vortex. Thus, if R_1 is a constant defined by $R_1^2 = \cot^2\xi_0 + \coth^2\chi_0$, corresponding to the starting position $(\xi_0, -\chi_0)$, then subsequent positions along a streamline (ξ, χ) are given by $\chi = -\text{arccoth}[(R_1^2 - \cot^2\xi)^{1/2}]$. In the case when $\xi_0 = \pi/2$, $R_1^2 = \coth^2\chi_0$. Some examples of paths followed for a selection of starting positions are shown in Fig. 4. The vortex is moved mainly under the influence of the nearest neighbor vortex in an anticlockwise sense around its cell, and the nearest point to the surface at $z = 0$ always occurs at $x = l/2$ (equal spacing, $\xi = \pi/2$), where the induced vertical velocity is zero. The vortex in the adjoining Langmuir cell ($-l \le x \le 0$, $-\infty \le z \le 0$) will have paths that are the mirror image of those in Fig. 4, circulating clockwise around the cell.

In a study of the formation of vortex pairs by wind gusts or breaking waves, Csanady (1994) used a four-vortex model composed of two real and two image vortices to show a similar effect. The paths determined from this four-vortex model $\chi = -R_1\xi/(\xi^2 - R_1^2)^{1/2}$ (see appendix A) are also shown in Fig. 4. It can be seen that provided that the influence from the vortex at $(2l - x_0, -z_0)$ is small (which is equivalent to $x_0 \le l/2$ and is the most likely scenario), the paths are very similar. In all cases the end result is the same, whether equally spaced or not. The vortices do not remain stationary but move away from their initial positions; any initial distribution consistent with that chosen is, in this sense, unstable. Thus, in the absence of continuous forcing or of dissipation that maintains their position near the water surface, a regular array or pair of vortices will migrate downward until their motion is impeded by the presence of the sea or lake bed or by their encounter with a thermocline as considered in the following sections.

6. A vortex model of Langmuir cells in finite depth

a. The general equations

The second case considered by Thorpe (1992) is shown in Fig. 5a. It has horizontal boundaries at $z = -h$ and 0 above and below the vortex array, the upper representing the water surface and the lower either a flat bottom or a thermocline (supposed rigid). The cell boundaries are still at horizontal positions $x = ml$, and there is convergence on the water surface ($z = 0$), leading to windrows at $x = 2ml$; the corresponding separation of windrows is $2l$. In this case, a doubly infinite array of image vortices is required to make the vertical velocity zero at the two boundaries; in addition to the array of equally spaced "real" vortices of circulation

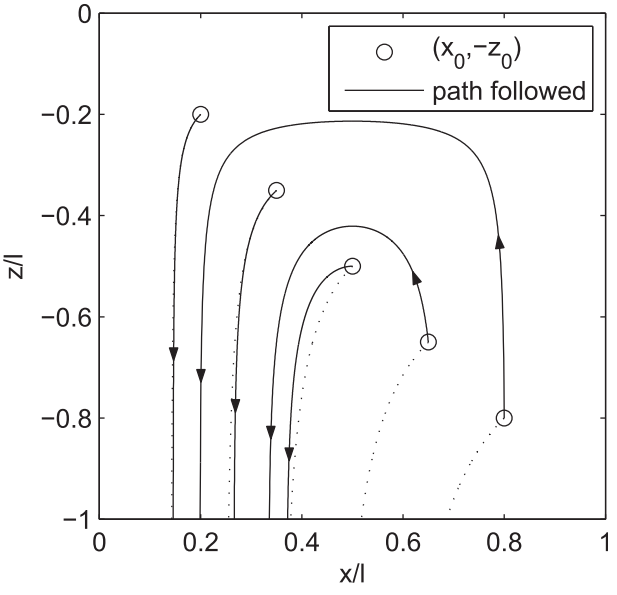

FIG. 4. Shows the paths followed by a vortex located at various starting positions $(x_0, -z_0)$, $z_0 = x_0$, where $x_0 = 0.2l$, $0.35l$, $0.5l$, $0.65l$, and $0.8l$, calculated according to Eq. (10). The isolated four-vortex solution is also shown as a dotted line calculated according to Eq. (A3), where $\xi = \pi x/l$ and $\chi = \pi z/l$.

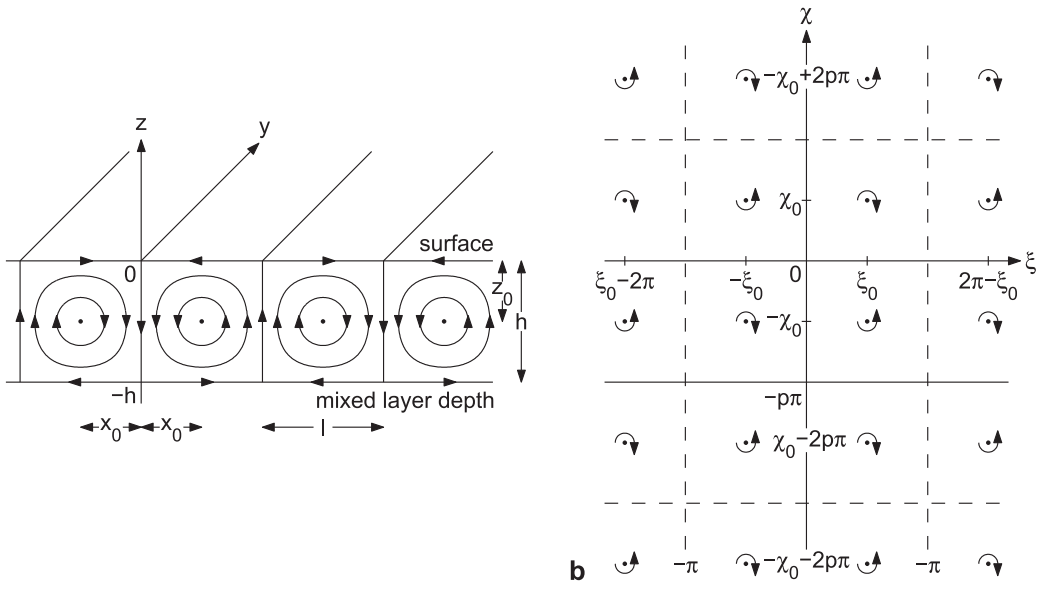

FIG. 5. Definition sketch of finite-depth Langmuir circulation for equal spacing (a) dimensional and (b) nondimensional in the complex ζ plane (solid horizontal lines at $\chi = 0$ and $-p\pi$ correspond to the water surface and base of mixed layer). The notation, using x_0, z_0, ξ_0, and χ_0, anticipates unequal spacing (equal spacing in the horizontal is given by $x_0 = l/2$ and $\xi_0 = \pi/2$, and equal spacing in the vertical is given by $z_0 = h/2$ and $\chi_0 = p\pi/2$).

$(-1)^{m+1}\Gamma$ at $x = (m + \frac{1}{2})l$, $z = -h/2$, image vortices of circulation $(-1)^{(m+n+1)}\Gamma$ are required at $x = (m + \frac{1}{2})l$, $z = (n - \frac{1}{2})h$, where m is an integer and n is an integer ranging from $-\infty$ to -1 and from 1 to ∞ to make the vertical velocity zero at the boundaries: $z = -h$ and 0. Following the same procedure as in section 5 (anticipating unequal spacing and nondimensionalization), all the vortices may be separated into four groups of arrays of like-signed circulations: Γ at $(2ml - x_0, 2nh - z_0)$, $-\Gamma$ at $(2ml + x_0, 2nh - z_0)$, $-\Gamma$ at $(2ml - x_0, 2nh + z_0)$, and Γ at $(2ml + x_0, 2nh + z_0)$, where n is an integer, or in the nondimensional ζ plane by $\zeta = -\zeta_0 + 2m\pi + np\pi i$, $\zeta_0^* + 2m\pi + np\pi i$, $-\zeta_0^* + 2m\pi + np\pi i$, and $\zeta_0 + 2m\pi + np\pi i$, with circulations Γ, $-\Gamma$, $-\Gamma$, and Γ (as shown in Fig. 5b), where $p = h/l$. Each bounded cell has dimensions $l \times h$ ($\pi \times p\pi$) regardless of the spacing of the vortices. The Thorpe case of equal spacing, both horizontally and vertically, then corresponds to the special case when $x_0 = l/2$ and $z_0 = h/2$ ($\xi_0 = \pi/2$ and $\chi_0 = p\pi/2$).

An expression for the horizontal velocity at ζ_0^* and $-\zeta_0$ in this finite-depth, equally spaced case can be inferred from generalizing Eq. (8) by realizing that the advective contribution from each array of image vortices is given by $\pm(-1)^n U/\sinh np\pi$, such that

$$u(\pm\pi/2 - ip\pi/2) = \pm U \sum_{\substack{n=-\infty \\ n\neq 0}}^{\infty} \frac{(-1)^n}{\sinh np\pi}, \qquad (11)$$

where the sum can be separated into sums from $-\infty$ to -1 and 1 to ∞, which exactly cancel one another, so that the vortices are indeed stationary in this case. By a similar argument Eq. (7) evaluated at $\xi = \pi/2$ can be generalized to determine the surface velocity at $\xi = \pi/2$ by recognizing that the contribution from all the vortices at $\pm(n + \frac{1}{2})p\pi i$ is $(-1)^{n+1}2U/\sinh(n + \frac{1}{2})p\pi$, where n is an integer ($0 \le n \le \infty$) such that

$$u(\pi/2) = -2U \sum_{n=0}^{\infty} \frac{(-1)^n}{\sinh(n + \frac{1}{2})p\pi}. \qquad (12)$$

This expression for $u(\pi/2)$ was used by Thorpe (1992) for scaling purposes to determine the strength of the circulation for comparison with observations.

In general, for unequally spaced vortices in the horizontal and vertical $\xi_0 \neq \pi/2$ and $\chi_0 \neq p\pi/2$ ($x_0 \neq l/2$ and $z_0 \neq h/2$), the four groups of infinite arrays, with circulations Γ, $-\Gamma$, $-\Gamma$, and Γ, centered at $\zeta = -\zeta_0 + i2np\pi$, $\zeta_0^* + i2np\pi$, $-\zeta_0^* + i2np\pi$, and $\zeta_0 + i2np\pi$, together have a complex potential given by

$$\Omega = i\frac{\Gamma}{2\pi} \sum_{n=-N}^{N} \log\left[\frac{\sin\frac{1}{2}(\zeta + \zeta_0 - i2np\pi)}{\sin\frac{1}{2}(\zeta - \zeta_0^* - i2np\pi)}\right] + i\frac{\Gamma}{2\pi} \sum_{n=-N}^{N-1} \log\left[\frac{\sin\frac{1}{2}(\zeta - \zeta_0 - i2np\pi)}{\sin\frac{1}{2}(\zeta + \zeta_0^* - i2np\pi)}\right], \qquad (13)$$

where $N \to \infty$. Here, the $n = 0$ terms in the two sums correspond to the potential in the infinite-depth case Eq. (5). The difference between the lower and upper limits in the second sum is required in anticipation of the finite

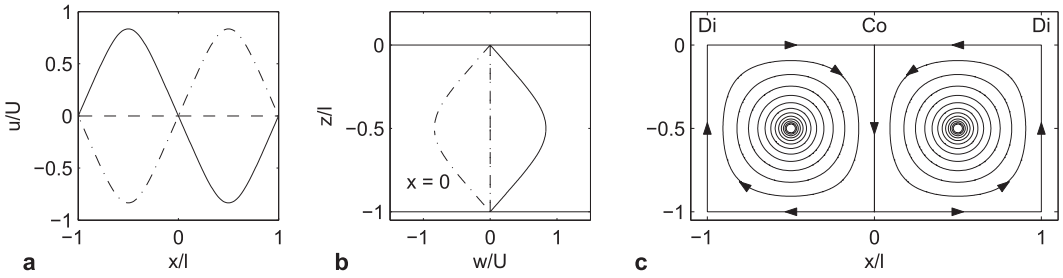

FIG. 6. Shows (a) u at $z = 0$ (solid), $-l/2$ (dashed), and $-l$ (dashed–dotted), (b) w at $x = -l$ (solid), $-x_0$ (dashed), 0 (dashed–dotted), and x_0 (dotted), where w at $x = \pm x_0$ lie on top of one another, and (c) the streamlines for stationary finite-depth Lc with square cells ($h = l$) for a vortex centered at $(x_0, -l/2)$, where $x_0 = l/2$, determined from Eqs. (14) and (13) with $\xi_0 = \pi/2$, $\chi_0 = \pi/2$, and $p = 1$.

sum approximations in the vertical, such that image rows above and below the domain must balance. From Eq. (13) and $u - iw = (\pi/l)d\Omega/d\zeta$, the velocity in the finite-depth case may be expressed as

$$u - iw = \frac{1}{2}U \times \begin{cases} i\sum_{n=-N}^{N} \cot^{1}\!/_{2}(\zeta + \zeta_0 - i2np\pi) - \cot^{1}\!/_{2}(\zeta - \zeta_0^* - i2np\pi) \\ +i\sum_{n=-N}^{N-1} \cot^{1}\!/_{2}(\zeta - \zeta_0 - i2np\pi) - \cot^{1}\!/_{2}(\zeta + \zeta_0^* - i2np\pi), & \zeta \neq \zeta_0^*, -\zeta_0, \\ \sum_{n=-N}^{N} i\cot(\xi_0 - inp\pi) - \sum_{n=-N}^{N-1} \coth(\chi_0 + np\pi) + i\cot(\zeta_0^* - inp\pi), & \zeta = \zeta_0^*, \\ \sum_{n=-N}^{N} i\cot(\xi_0 + inp\pi) + \sum_{n=-N}^{N-1} \coth(\chi_0 + np\pi) - i\cot(\zeta_0 + inp\pi), & \zeta = -\zeta_0, \end{cases} \tag{14}$$

where $U = \Gamma/2l$. Figure 6 shows the horizontal and vertical velocity and streamlines for the stationary case, with $\xi_0 = \pi/2$, $\chi_0 = p\pi/2$, and $p = 1$, determined from Eqs. (14) and (13). Figure 6 can be compared to the infinite-depth case (Fig. 2). In addition to the flow being depth limited, it is also symmetric about the line $z = -l/2$ ($\chi = -\pi/2$), in such a way that when the cell edge on the upper surface has a convergence, the lower surface has an equal and opposite divergence and vice versa. It can be shown that when $N \to \infty$ in Eq. (14), the velocity evaluated at the surface, $\zeta = \xi$, $u(\xi)$, is given by

$$u(\xi) = -2U\sin\xi_0\left(\frac{C_{10}}{B_{10}^2 + C_{10}^2} + \sum_{n=1}^{\infty}\frac{C_{1n}}{B_{1n}^2 + C_{1n}^2} - \frac{C_{2n}}{B_{2n}^2 + C_{2n}^2}\right), \tag{15}$$

where B_{1n} and $B_{2n} = \cos\xi_0 - \cos\xi\cosh(2np\pi \pm \chi_0)$, and C_{1n} and $C_{2n} = \sin\xi\sinh(2np\pi \pm \chi_0)$. Here, the first term is the result of the infinite-depth solution [Eq. (9)]. When $\xi = \xi_0 = \pi/2$, Eq. (15) reduces to

$$u(\pi/2) = -2U\left[\frac{1}{\sinh\chi_0} + \sum_{n=1}^{\infty}\frac{1}{\sinh(2np\pi + \chi_0)} - \frac{1}{\sinh(2np\pi - \chi_0)}\right], \tag{16}$$

and when $\chi_0 = p\pi/2$, by separating the sum into odd and even terms in n, Eq. (16) reduces to Eq. (12).

b. *Small-amplitude perturbations*

The Thorpe case of equal spacing, both horizontally and vertically, is given by $x_0 = l/2$ and $z_0 = h/2$ ($\xi_0 = \pi/2$ and $\chi_0 = p\pi/2$). Thorpe (1992) considers spatially periodic perturbations to the real array of line vortices (with reciprocal perturbations in their images to maintain zero vertical velocity at $\chi = -p\pi$ and 0) in both the ζ plane and in the along-vortex line direction y, when vortices are represented with finite cores (as in Crow 1970). Two modes of instability of the vortex lines are favored, having the greatest growth rates. When $p \ll 1$ ($p = h/l$), vortices oscillate collectively with the nonzero along-axis wavenumber. When p is large vortices are involved in ''pairing.'' The latter generally has the greater growth rates with the most rapid growth corresponding to a disturbance with an along-vortex (or downwind) scale of about 4.6 to 8.1 times the windrow separation; rates increase as the windrow spacing decreases in comparison with the depth h. Although broadly consistent to the ratios L_0/s for the downwind length of cells found in the observations and LES models, these exceed the ratios L_1/s

for the length of continuous patches to which they might be expected to be more closely related.

A further infinitesimal, two-dimensional perturbation, one independent of y, can be examined by supposing that vortices of circulation $(-1)^{(m+n+1)}\Gamma$ are moved symmetrically within the fixed boundaries of a set of Langmuir cells to nondimensional positions $\xi = (m + \frac{1}{2})\pi + (-1)^m a$ and $\chi = (n - \frac{1}{2})p\pi + (-1)^n b$, where a and b are small. Summing over the vortex array, using Eq. (3) to find the velocity induced at the vortex with $m = n = 0$ located at $(\pi/2 + a, -p\pi/2 + b)$, and neglecting terms of order a^2 and b^2, the horizontal and vertical velocities $da/d\tau$ and $db/d\tau$, where τ is the nondimensional time $(=\pi Ut/l)$, are found to be (see appendix B)

$$\frac{da}{d\tau} = -\frac{Ab}{2p^2}, \quad \frac{db}{d\tau} = \frac{Ba}{2}, \tag{17a,b}$$

where A and B are

$$A = 1 + 2\sum_{m=1}^{\infty}(-1)^m \operatorname{sech}^2(m\pi/2p), \quad \text{and} \tag{18a}$$

$$B = 1 + 2\sum_{n=1}^{\infty}(-1)^n \operatorname{sech}^2(n\pi p/2). \tag{18b}$$

Solutions for a and b are proportional to $e^{\sigma\tau}$, where

$$\sigma^2 = -\frac{AB}{4p^2}. \tag{19}$$

It may be shown that $\sigma^2 < 0$ for all p $(=h/l)$. [Although the sum terms in Eqs. (18a) and (18b) are negative for all p, they asymptote to a minimum of -1.0 from above as $p \to 0$ and $p \to \infty$, where consequently σ tends to zero.] The growth rate of perturbations σ is therefore imaginary. Solutions are periodic corresponding to neutrally stable modes in which vortices move steadily around closed elliptical orbits with a b/a aspect ratio of $p(B/A)^{1/2}$ (circular if $p = 1$) circumscribed in a time of $\tau_p = 2\pi/|\sigma| = 4\pi p/(AB)^{1/2}$. Thus, the period of oscillation T is given by

$$T = \left(\frac{l}{\pi U}\right)\frac{4\pi p}{\sqrt{AB}}. \tag{20}$$

Summing the rapidly converging series in Eqs. (18a) and (18b) numerically, this period of a vortex perturbed from a position in the center of a cell is found to be equal to $18.04(l/\pi U)$ when $p = 1$, that is, for the roughly square cells observed by Smith (1998). This can be compared with the period of a particle to orbit around a stationary vortex T_o, starting at a distance r away from the vortex. It can be anticipated that $r < l/2$, for example, when $r = 0.47l$, $T_o = 1.339(\pi 15/16)^2 l^2/\Gamma$ (see appendix C), so that $T_o/T = 1.339\pi(\pi 15/16)^2/36.08 = 1.01 \sim 1$ or $T_o < T$. For $r \ll l$, $T_o \sim (2\pi r)^2/\Gamma$ (see appendix C), so that $T_o/T = (4\pi^3/36.08)(r/l)^2$, such that, for example, if $r = l/10$, the particle period is $T_o/T \sim 0.034$. The displaced vortices therefore move relatively much less rapidly around the center of a Langmuir cell than do particles close to a stationary vortex at the cell center. Thus, a particle's motion consists of loops around the vortex's circular path.

But what of vortices subjected to finite perturbations from the center of the Langmuir cells?

c. *Nonstationary vortices: Vacillation*

The infinitesimal perturbation approach used in section 6b demonstrated that vortices could undergo repeatable orbits around the stationary center. The equivalent can be demonstrated for finite perturbations by calculating the vortex streamfunction, as in the infinite-depth case. This has been done in appendix D, where it is shown that $\psi(\zeta_0^*)$ can be approximated by

$$\psi(\zeta_0^*) = -\frac{\Gamma}{4\pi}\log\left[(\cot^2\xi_0 + \coth^2\chi_0)\prod_{n=1}^{2}\frac{P_n^2 + Q_n^2}{R_{1n}^2 R_{2n}^2}\right], \tag{21}$$

where $P_n = -(1 - \coth^2 np\pi \coth^2\chi_0) - R_{2n}\cot^2\xi_0$, $Q_n = 2(1 - \coth^2 np\pi)\cot\xi_0 \coth\chi_0$, $R_{1n} = (\coth^2 np\pi + \cot^2\xi_0)$, and $R_{2n} = (\coth^2 np\pi - \coth^2\chi_0)$. Thus, as with Eq. (10), if $\psi(\zeta_0{}^*)$ and hence the square-bracketed term remains constant from a starting position $(\xi_0, -\chi_0)$ to all subsequent positions (ξ,χ) then the resulting curve corresponds to the path of the vortex. Figure 7a shows orbits based on the contours of Eq. (21) for a square cell: $h/l = p = 1$. The vortex circulates anticlockwise around the cell $(0 \le x \le l, -l \le z \le 0)$ in closed orbits that are centered about $(l/2, -l/2)$, the stationary center corresponding to Thorpe's (1992) equal spacing. The vortex in the $(-l \le x \le 0, -l \le z \le 0)$ cell will have paths that are the mirror image of those in Fig. 7a, circulating clockwise. Thus, depending on where the vortex is relative to its nearest neighbor will determine whether the convergence is stronger, the divergence is stronger, or the convergence and divergence are of equal strength. Therefore, unlike the infinite-depth case, in the finite-depth case, a dynamic Lc pattern can persist.

More generally when $h/l \neq 1$, the orbit of the vortex can be described by its quadrants: it starts at $(l/2, -z_0)$ at 90°, then on to $(x_{\min}, -h/2)$ at 180° ($x_{\min}$ corresponds to half the closest horizontal distance that a vortex in the real array comes to its nearest neighbor, as defined in Fig. 7a), $(l/2, z_0 - h)$ at 270°, and $(l - x_{\min}, -h/2)$ at 360° (or 0°) before returning to $(l/2, -z_0)$

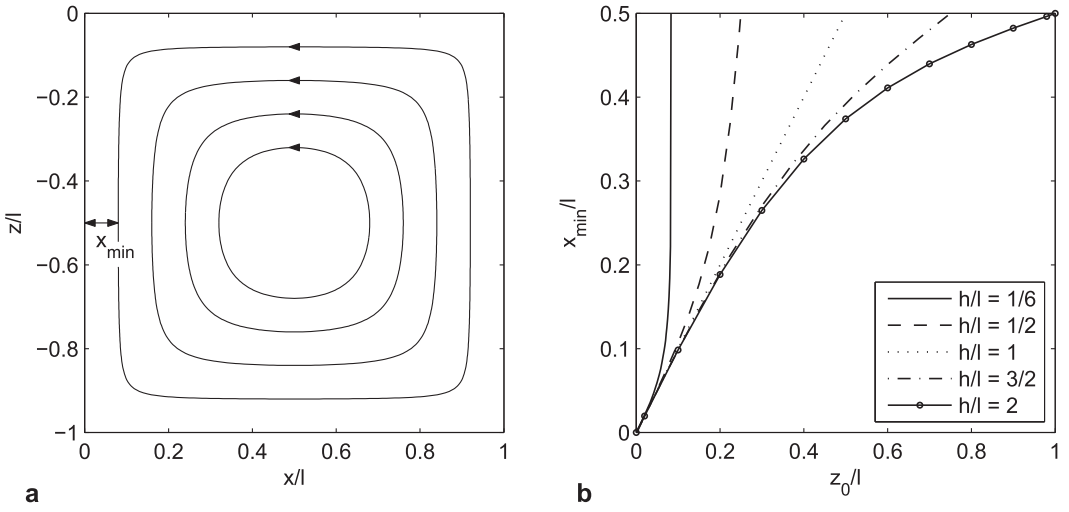

FIG. 7. (a) Shows the possible paths followed by a vortex for finite-depth Lc with a square cell ($h/l = 1$). The paths correspond to the vortex starting at $(l/2, -z_0)$, where $z_0 = 0.08l$, $0.16l$, $0.24l$, and $0.32l$, as determined from Eq. (21) with $\xi = \pi x/l$, $\chi = \pi z/l$, $\xi_0 = \pi/2$, $\chi_0 = \pi z_0/l$, and $p = 1$. Half the closest horizontal distance that a vortex comes to its nearest (real) neighbor $x_{\min}$ is marked for the outmost path (for which $x_{\min} = 0.08l$, since $x_{\min} = z_0$ when $h/l = 1$). (b) Shows the variation $x_{\min}$ with the z_0, for $h/l = 1/6$, $1/2$, 1, $1\frac{1}{2}$, and 2.

(see Fig. 7a). Thus, $x_{\min}$ and z_0 can be used to define a box $x_{\min} \le x \le l - x_{\min}$, $z_0 - h \le z \le -z_0$ within the cell that contains the vortex path. The variation in $x_{\min}$ with z_0 is shown in Fig. 7b for $h/l = 1/6$, $1/2$, 1, $1\frac{1}{2}$, and 2 ($h/l = p$). It can be seen that $x_{\min}$ depends on both z_0 and h/l. Notice that only in the $h/l = 1$ case does $x_{\min} = z_0$ (as shown in Fig. 7a) because of the symmetry of this particular setting (when $h/l < 1$, $x_{\min} > z_0$ and when $h/l > 1$, $x_{\min} < z_0$).

Using the velocity in Eq. (14) approximated by taking a finite number of terms, $N = 10$ or 100, and a small advective time step, it is possible to calculate the time taken for one-quarter of a revolution of the vortex $T_{1/4}$ from a starting point at $(l/2, -z_0)$ or 90° around to a finishing

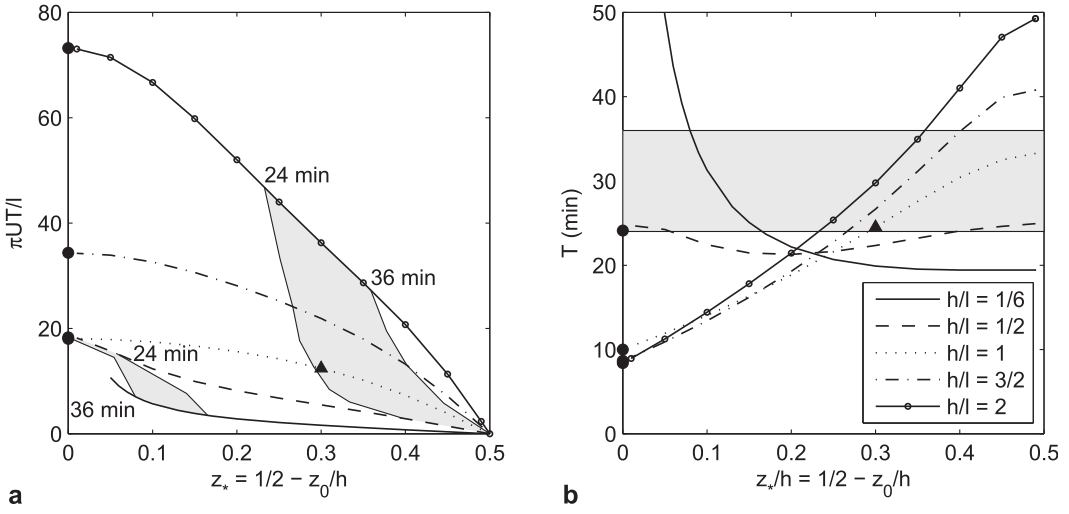

FIG. 8. Variation in (a) the nondimensional period $\pi UT/l$ and (b) the dimensional period T for a vortex to undertake a complete revolution around its path with the perturbation amplitude z_* for $h/l = 1/6$, $1/2$, 1, $1\frac{1}{2}$, and 2 (the finite calculation; section 6c). Solid circles show the infinitesimal perturbation analysis period (section 6b). For clarity, no results for $z_* < 0.05h$ are shown for the $h/l = 1/6$ case. The shaded regions corresponds to the allowable values of z_0, where T is in the range $24 \le T \le 36$ min, using a scaling based on $|u(\pi/2)| = 0.2\ \mathrm{m\ s^{-1}}$ and $l = 25$ m in Eq. (16). The solid triangle corresponds to the example case shown in Figs. 9 and 10.

TABLE 1. Vacillation period T in minutes for shallow water $h = 15$ m.

	$\lvert u(\pi/2)\rvert = 0.1\ \mathrm{m\,s^{-1}}$		$\lvert u(\pi/2)\rvert = 0.2\ \mathrm{m\,s^{-1}}$	
l (m); p (−)	$z_* \sim h/2$	$z_* = 0.05h$	$z_* \sim h/2$	$z_* = 0.05h$
90; 1/6	140	358	70	179
45; 1/3	80	135	40	67

point $(x_{\min}, -h/2)$ or 180°. The period of revolution is then simply $T = 4T_{1/4}$. Figure 8a shows $\pi UT/l$ versus the perturbation amplitude $z_* = h/2 - z_0$ for the same values of h/l shown in Fig. 7b (⅙, ½, 1, 1½, and 2). For clarity, because the period rises rapidly to $\pi UT/l = 1081$ at $z_* = 0$ (section 6b), the $h/l = ⅙$ case is not shown for $z_* < 0.05h$. The maxima in $\pi UT/l$ as $z_* \to 0$ are 1079, 18.20, 18.08, 34.28, and 73.06 for these values of h/l. This is very close to the T calculated from the infinitesimal perturbation analyses [Eq. (20)] $\pi UT/l = 1081$, 18.31, 18.04, 34.36, and 73.24, which, except for the $h/l = ⅙$ case, are shown in Fig. 8a by solid circles. The fact that the nondimensional period appears very similar for $h/l = ½$ and 1 is an artifact of the scaling as will be seen next.

We interpret the fluctuations caused as a vortex moves around its orbit as the source of vacillations. The peak convergence velocity in vacillations of Smith (1998) was $0.2\ \mathrm{m\,s^{-1}}$ (section 2c), which corresponds to $\lvert u(\pi/2)\rvert = 0.2\ \mathrm{m\,s^{-1}}$ in Eq. (16). [Although in the model with $p = 1$ the maximum vertical and horizontal velocities are equal, this speed exceeds the vertical downwelling speed of 0.006–0.01 times the 10-m wind speed found by Li and Garrett (1993) in the absence of vacillations.] Together with $l \sim 25$ m, knowledge of the convergence speed allows U to be determined in terms of z_0 (χ_0) resulting in the period T, shown in Fig. 8b. For a fixed $\lvert u(\pi/2)\rvert$ in Eq. (16), the strong decrease in U with increasing $z_* = h/2 - z_0$ causes T to increase when $h/l > ½$. Bearing in mind Smith's (1998) observed vacillations of period $T \sim 30$ min, a shaded region corresponding to T being in the range of uncertainty $24 \le T \le 36$ min and allowable values of z_* are also shown in Figs. 8a and 8b. It can be seen that this range of periods for the vacillation and maximum velocity is only achieved when the vortex perturbation is greater than half the distance between the stationary center and the surface $z_0 < h/4$, except in the case of $h/l = ½$, which has an additional region close to the stationary center and the $h/l = ⅙$ case, which only has a region close to the stationary center. The $h/l = ⅙$ case is included because it represents the smallest aspect ratio of shallow-water Langmuir supercells (LSC), which extend over the full-water depth (Gargett and Wells 2007). Assuming $p = ⅙$ and a vacillation with $\lvert u(\pi/2)\rvert = 0.1\ \mathrm{m\,s^{-1}}$ in Eq. (16), and $l = 90$ m (6 times the water depth in Gargett and Wells study and their maximum size of Langmuir cells), the vacillation period is much longer varying from 140 min when the perturbation amplitude $z_* \sim h/2$ to 358 min when $z_* = 0.05h$. The range in vacillation periods in water of 15-m depth, for $\lvert u(\pi/2)\rvert = 0.1$ and $0.2\ \mathrm{m\,s^{-1}}$ and $p = ⅙$ and ⅓, is given in Table 1. It can be seen that this period is always greater than 30 min.

Figures 9a–f show an example case of the instantaneous streamlines for a square cell ($h/l = 1$) where the vortex starts at $(l/2, -l/5)$, which is in the allowable range according to Figs. 8a and 8b and rotates one-quarter of a cycle, passing one corner of the Langmuir cell. Similar orbits will be found in the other corners. Based on the values of t/T for each vortex position (stated in the figure caption), it can be seen that the vortex slows down as it passes the corner. This is because the vortex responds mainly to its nearest neighbor and control is changing from the image vortex above the surface at (x_0, z_0) to the real vortex in the neighboring cell at $(-x_0, -z_0)$. The most likely position for a vortex to be observed is where it moves most slowly, that is, near the corner of a Langmuir cell. The instantaneous streamlines are centered on the local position of the vortex. This would suggest that fluid particles move along these streamlines in an anticlockwise sense. However, as will be seen in the next figure, the particle motions are more complex than this.

Also shown in Fig. 9g is the manifestation of the vacillation associated with the movement of the vortex around half its orbit (from 90° to 270°) as seen in the surface velocity according to Eq. (15) ($U = 0.067\ \mathrm{m\,s^{-1}}$). The velocity is negative toward the nearest windrow at $x = 0$, and the minimum in the velocity reflects the horizontal position within the cell (in the other half of the orbit the profiles of the velocity at 315°, 360°, and 45° will be the mirror images of the 225°, 180°, and 135° about the $x = l/2$ line). For comparison, the dotted line corresponds to the surface velocity in the case of the vortex at the stationary center [Eq. (15), with $\xi_0 = \pi/2$, with $\chi_0 = -p\pi/2$]. The ratio of the strongest velocity relative to the weakest velocity as determined by the 90° and 270° minima at $x = l/2$ is $2.973/0.234 \sim 12.7$ in this case [the minima can be determined using Eq. (16) with $\chi_0 = \pi/5$ and $4\pi/5$], so the convergence velocity vacillates between 0.016 and $0.20\ \mathrm{m\,s^{-1}}$. From Eq. (12) the minimum surface velocity in the stationary case is $0.8346U$, which is equivalent to $0.056\ \mathrm{m\,s^{-1}}$. The convergence and divergence in the surface velocity at $x = 0$ and l can be determined from the derivative of Eq. (15) evaluated at $\xi = 0$ and π, respectively:

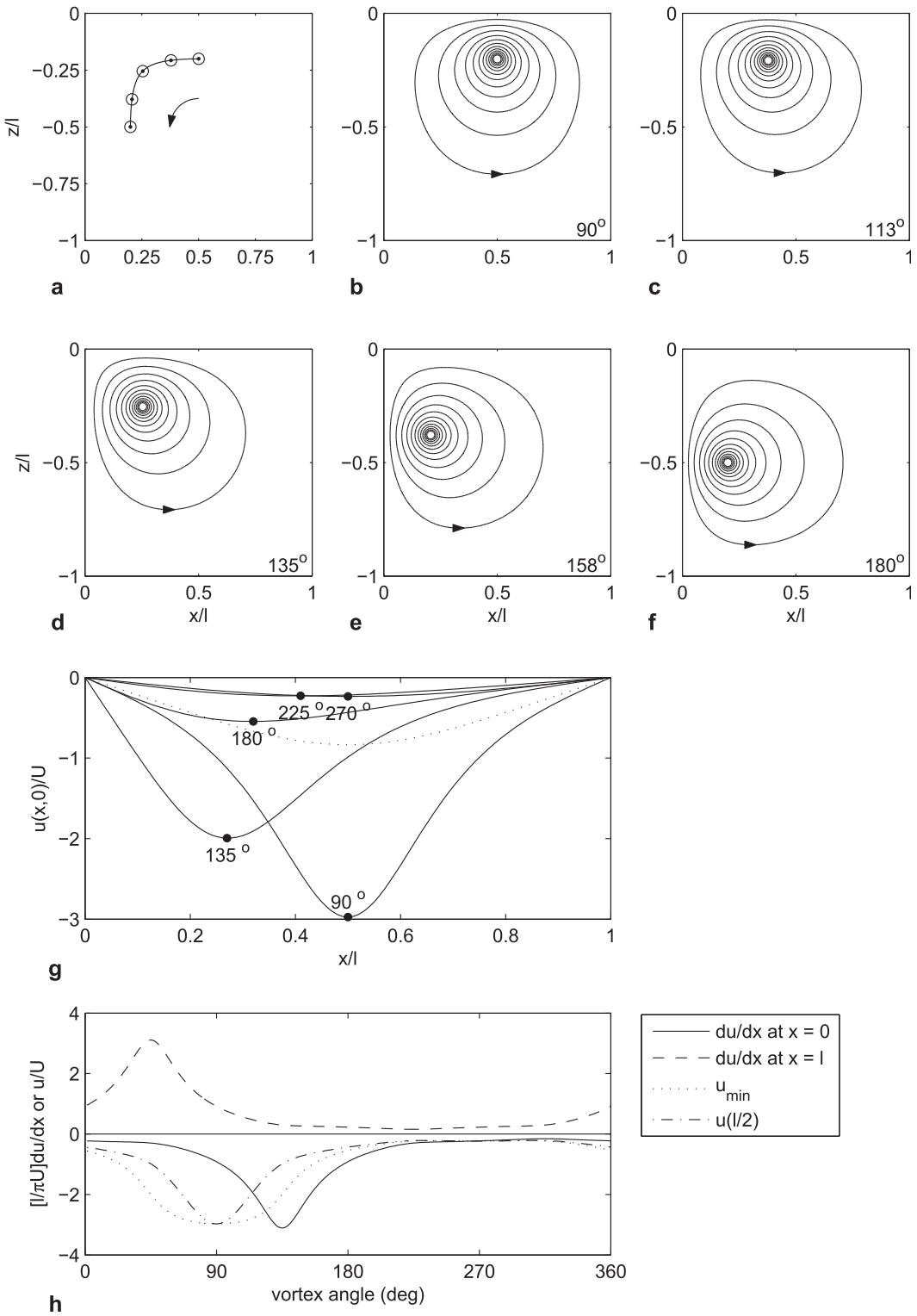

FIG. 9. (a) Selection of vortex locations over a quarter of one revolution starting at ($l/2$, $-l/5$) and (b)–(f) the corresponding instantaneous streamlines for the flow (the angles around the path, given in the bottom right-hand corner of each subplot correspond to $t/T = 0, 0.0522, 0.1250, 0.1978$, and 0.2500). (g) The horizontal surface velocity over one-half of a revolution of the vortex, as determined by Eq. (15) with $\xi = \pi x/l$, $\xi_0 = \pi x_0/l$, $\chi_0 = \pi z_0/l$, and $p = 1$. The solid circles mark the minima for each case, and the dotted line corresponds to the surface velocity in the stationary case, Eq. (15) with $\xi_0 = \pi/2$, $\chi_0 = \pi/2$, and $p = 1$. (h) The convergence and divergence at $x = 0$ and l based on Eq. (22), the minimum in the surface velocity $u_{\min}$, and the velocity at $l/2$, $u(l/2)$, over a complete revolution of the vortex.

$$\frac{du}{dx} = \frac{2\pi U}{l}\sin\xi_0 \times \begin{cases} -\dfrac{C'_{10}(0)}{B^2_{10}(0)} - \displaystyle\sum_{n=1}^{\infty}\frac{C'_{1n}(0)}{B^2_{1n}(0)} - \frac{C'_{2n}(0)}{B^2_{2n}(0)}, & \xi = 0, \\ \dfrac{C'_{10}(0)}{B^2_{10}(\pi)} + \displaystyle\sum_{n=1}^{\infty}\frac{C'_{1n}(0)}{B^2_{1n}(\pi)} - \frac{C'_{2n}(0)}{B^2_{2n}(\pi)}, & \xi = \pi, \end{cases} \tag{22}$$

where $B_{1n}(0)$ and $B_{2n}(0) = \cos\xi_0 - \cosh(2np\pi \pm \chi_0)$, $B_{1n}(\pi)$ and $B_{2n}(\pi) = \cos\xi_0 + \cosh(2np\pi \pm \chi_0)$, and $C'_{1n}(0)$ and $C'_{2n}(0) = \sinh(2np\pi \pm \chi_0)$. The convergence at $x = 0$ and the divergence at $x = l$ are shown in Fig. 9h, together with the minimum in the surface velocity and the surface velocity at $x = l/2$, versus the vortex angle. It can be seen that convergence and divergence are strongest when the vortex is closest to the appropriate corner, at 45° and 135°, respectively. The convergence is strongest at angles between 90° and 270°, when the vortex is closer to the $x = 0$ than the $x = l$ line, and the divergence is strongest at other angles (the convergence and divergence are equal in strength when the vortex is equidistant from the $x = 0$ than the $x = l$ lines, at 90° and 270°). Since the Langmuir cell is square, the downwelling velocity at $(0, -l/2)$ will be the same as the surface velocity at $x = l/2$, except that it will be delayed by 90°, such that it is strongest at 180°.

Figure 10 shows the same case depicted in Fig. 9, where the vortex starts at $(l/2, -l/5)$ over a complete cycle. The figure also shows the paths followed by 16 particles placed initially at different locations within the cell. (The center of the vortex also delineates a particle path.) A wide variety of particle paths is possible and most bear very little resemblance to the instantaneous streamlines shown in Fig. 9. Particle paths are generally not closed. They appear to be of several types. If a particle starts from a location near a vortex (e.g., Figs. 10f,j), it remains close to the vortex, performing multiple loops around its (moving) position. Such trapping may occur when the speed of the particle u_r at radius r from the vortex and driven by its motion significantly exceeds the speed of the vortex; for example, see the trapping within streamlines of a vortex pair in a mean flow illustrated in Fig. 7.3.3 of Batchelor (2000). The condition for trapping is approximately that the orbital period $T_o < T$. For a given vortex track, the number of particle loops per vortex orbit, about 16–17 in the examples in Figs. 10f and 10j, will increase as the initial distance r of a particle from the vortex decreases. In the case of Figs. 10f and 10j, where $r = l/10$, $T_o = 1.37(\pi/5)^2 l^2/\Gamma$ (see appendix C), and from Fig. 8a, $T = (28/\pi)l^2/\Gamma$ such that $T/T_o = 700/1.37\pi^3 = 16.4 \sim 16.5$, the observed number of orbits. Since the vortex speed is smallest near the corners of the Langmuir cell, it is here that escape from trapping is most likely to occur. A second type of trapping is shown in Figs. 10a, 10b, 10m, and 10n, where particles are carried to the edges of the cell. [Both types of trapping differ from that discovered and described by Stommel (1949), in which dense sinking particles can be maintained in suspension by the circulation within a Langmuir cell.] In the majority of cases illustrated in Fig. 10, the particle paths follow a single loop with dimensions comparable to that of the vortex path.

7. Discussion

Three types of breakdown of Langmuir circulation (Lc) have been observed (section 2). Two are identified in large-eddy simulation (LES) models, but the third, vacillation, is not (section 3). The vortex motion in Langmuir cells is represented here by line vortices and their images (section 4 onward).

The equally spaced line vortices in Thorpe's (1992) configuration chosen to represent Lc in the infinite-depth case (section 5) are not stationary, and consequently in this case his stability analysis is shown to be invalid, although the motion of vortices is shown to be similar to that examined by Csanady (1994) to explain the formation of Lc.

In section 6, attention is focused on the development of instability in Lc in water of limited depth. A set of vortices of alternating sign but equal strength at the center of cells of height h and width l is shown to be stationary (section 6a). Vortices perturbed by a small distance from their stationary locations move around these locations in elliptical orbits (section 6b); the configuration is neutrally stable. Finite-amplitude perturbations result in vortices that follow repeatable orbits producing variable convergence at the water surface (and hence variations of the efficiency of convergent motion to generate and sustain bubble bands) with a period equal to that of the vortices in their orbits, a process that we propose represents vacillation (section 6c). This vortex-related vacillation is different to the vacillation described by Tandon and Leibovich (1995). The periodicity of vortices in these orbits is found and is shown to be consistent with that during the vacillation observed by Smith (1998). Particle motions within Langmuir cells during vacillation are illustrated in Fig. 10. They are of three types. Particles close to an orbiting vortex are trapped and circle around it. Some particles are trapped near the cell boundaries, but most

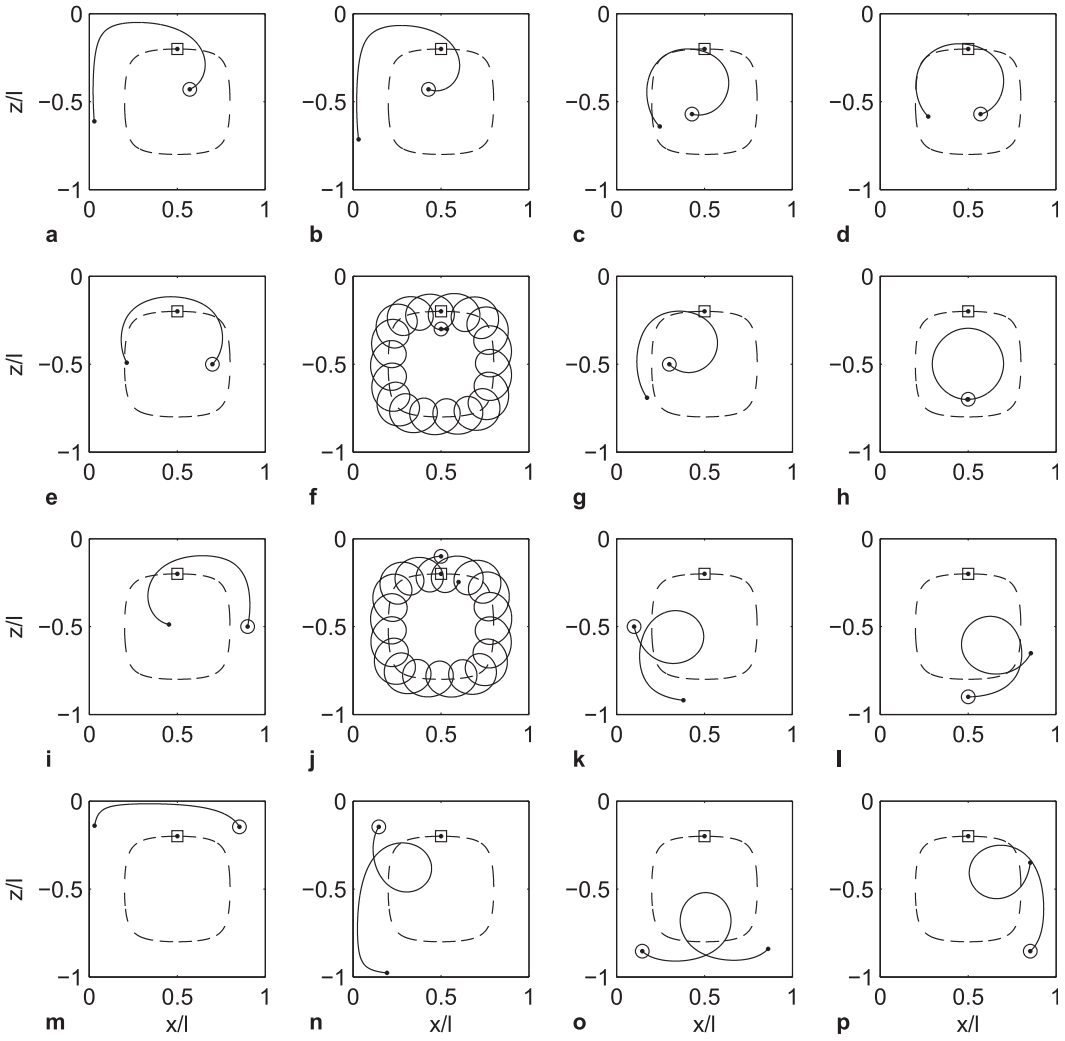

FIG. 10. (a)–(p) Selection of 16 particles placed at different starting locations within the cell (circled dot) and their paths followed (solid line), to their final position at the dot, in response to one complete revolution of the vortex for the case depicted in Fig. 9 stating at 90° (square on dot) around the path, shown as the dashed line. Both vortices and particles circulate anticlockwise.

particles follow loops of scale similar to the vortex's orbit.

Although the motion of vortices around their orbits results in perturbations similar to those observed by Smith during vacillation, in particular fluctuations in surface convergence that will result in stronger and weaker bubble bands, so accounting for the variations from relatively disorganized to intense and regular features, the 8% variation he reports in the mean separation of bands is not explained nor has a mechanism been found to explain the perturbation of vortices from a stationary state. Some yet unidentified process, such as the nearby breaking of a rogue wave or some effect associated with the fall in wind speed and change in its direction that followed Smith's observation of vacillation, is required to perturb the vortex motion within the Langmuir cells. More observations are needed to establish the nature and onset of vacillation.

No vacillation appears to have been observed in shallow water where $p = h/l$ is substantially smaller than the $p \sim 1$ value found in deep water by Smith (1998). The vacillation periods predicted in section 6c and given in Table 1 are longer than the 30-min period observed by Smith. For example with $p = 1/6$ and $|u(\pi/2)| = 0.1\,\mathrm{m\,s^{-1}}$, the vacillation period exceeds 2 h. It is rare that wind and wave forcing conditions remain constant over long periods and unlikely that the motion will then be independent of Earth's rotation. Vacillation in shallow water, detectable only

if it continues over several periods, is therefore less likely to be observed.

The representation of Lc by line vortices and their images is an approximation and neglects, for example, the effects of viscosity, small-scale turbulence or the finite dimensions of vortices, but it does provide a means to examine the stability of regular arrays of vortices and is a useful guide to further investigation.

Acknowledgments. This work was funded by the U.K. Natural Environment Research Council (NERC) under the COHBED (NE/1027223/1) project. We are grateful to Dr. J. A. Smith for his advice about the maximum surface flows during vacillation.

APPENDIX A

The Isolated Four-Vortex Model

The complex potential for the isolated four-vortex model, as proposed by Csanady (1994), where the vortices are centered at $\zeta = -\zeta_0$, ζ_0^*, $-\zeta_0^*$, and ζ_0 with circulations Γ, $-\Gamma$, $-\Gamma$, and Γ, respectively (see Fig. A1), is

$$\Omega = i\frac{\Gamma}{2\pi}\log\left(\frac{\zeta+\zeta_0}{\zeta-\zeta_0^*}\right) + i\frac{\Gamma}{2\pi}\log\left(\frac{\zeta-\zeta_0}{\zeta+\zeta_0^*}\right). \tag{A1}$$

The vortex streamfunction is $\psi(\zeta_0^*) = \mathrm{Im}[\Omega(\zeta_0^*)]$, where $\Omega(\zeta_0^*)$ is given by Eq. (A1) evaluated at $\zeta = \zeta_0^*$, with the self-potential removed. The term $\Omega(\zeta_0^*) = i(\Gamma/2\pi)\log(-i2\xi_0\chi_0/\zeta_0^*)$, so that $\psi(\zeta_0^*)$ is then

$$\psi(\zeta_0^*) = -\frac{\Gamma}{4\pi}\log\left(\frac{\xi_0^2+\chi_0^2}{4\xi_0^2\chi_0^2}\right). \tag{A2}$$

As with Eq. (10), if $R_1 = \xi_0\chi_0/(\xi_0^2 + \chi_0^2)^{1/2}$ [which is equivalent to Csanady's (1994) expression] corresponds to the starting position $(\xi_0, -\chi_0)$, then subsequent positions (ξ, χ) along a streamline are given by

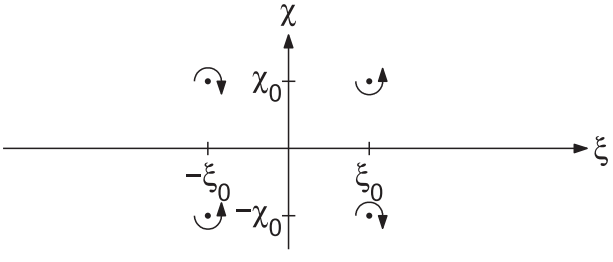

FIG. A1. Definition sketch for isolated four-vortex model in the nondimensional complex ζ plane.

$$\chi = -\frac{R_1\xi}{\sqrt{\xi^2 - R_1^2}}. \tag{A3}$$

APPENDIX B

Determining *A* and *B* in Eqs. (18a) and (18b)

From Eq. (3), the contribution of the m, n vortex at location $\xi = (m + \tfrac{1}{2})\pi + (-1)^m a$ and $\chi = (n - \tfrac{1}{2})p\pi + (-1)^n b$, with circulation $(-1)^{(m+n+1)}\Gamma$, to the $m = n = 0$ vortex, located at $(\pi/2 + a, -p\pi/2 + b)$, $u_{mn} - iw_{mn}$ is

$$u_{mn} - iw_{mn} = \frac{iU(-1)^{n+m}}{\pi(m+inp)+\Delta_{mn}} \approx iU(-1)^{n+m}\left[\frac{1}{\pi(m+inp)} - \frac{\Delta_{mn}}{\pi^2(m+inp)^2}\right], \tag{B1}$$

where $U = \Gamma/2l$ and $\Delta_{mn} = [(-1)^m - 1]a + i[(-1)^n - 1]b$. Since $da/d\tau$ and $db/d\tau$ are the sums of u_{mn}/U and of w_{nm}/U, respectively, over all m and n from $-\infty$ to ∞, only terms involving even powers of n and m in Eq. (B1) contribute to $da/d\tau$ and $db/d\tau$:

$$\frac{da}{d\tau} - i\frac{db}{d\tau} = -\sum_{n=-\infty}^{\infty}\sum_{m=-\infty}^{\infty} i\Delta_{mn}\frac{(-1)^{n+m}[m^2-(np)^2]}{\pi^2[m^2+(np)^2]^2}. \tag{B2}$$

Also, because these remaining terms in Eq. (B2) require either n or m to be odd for the real or imaginary parts of $i\Delta_{mn}$ to be nonzero, $da/d\tau$ and $db/d\tau$ can be written in terms of $2(n + \tfrac{1}{2})$ and $2(m + \tfrac{1}{2})$ as

$$\frac{da}{d\tau} = -\frac{b}{2p^2}\sum_{m=-\infty}^{\infty}(-1)^m\sum_{n=-\infty}^{\infty}\frac{(n+\tfrac{1}{2})^2-(m/2p)^2}{\pi^2[(n+\tfrac{1}{2})^2+(m/2p)^2]^2}, \tag{B3a}$$

and

$$\frac{db}{d\tau} = \frac{a}{2}\sum_{n=-\infty}^{\infty}(-1)^n\sum_{m=-\infty}^{\infty}\frac{(m+\tfrac{1}{2})^2-(np/2)^2}{\pi^2[(m+\tfrac{1}{2})^2+(np/2)^2]^2}. \tag{B3b}$$

The sums over n and m in Eqs. (B3a) and (B3b), which are well known in stability analysis (see, e.g., Robinson and Saffman 1982), are given by $\mathrm{sech}^2(m\pi/2p)$ and $\mathrm{sech}^2(n\pi p/2)$, respectively. Thus, by defining Eqs. (B3a) and (B3b) as $da/d\tau = -Ab/2p^2$ and $db/d\tau = Ba/2$, A and B are

$$A = 1 + 2\sum_{m=1}^{\infty}(-1)^m\,\mathrm{sech}^2(m\pi/2p), \quad \text{and} \tag{B4a}$$

$$B = 1 + 2\sum_{n=1}^{\infty}(-1)^n \operatorname{sech}^2(n\pi p/2). \qquad \text{(B4b)}$$

APPENDIX C

Particle Periods around a Fixed Vortex in Finite-Depth Lc

The period for one complete orbit T_o for a particle placed at various starting positions $(l/2, z)$ in a square Lc cell ($h = l$) in response to a fixed vortex placed at $(l/2, -z_0)$, where $z_0 = l/2$ (the true stationary position) and $z_0 = l/5$ (the example starting position in Figs. 9 and 10), are shown in Fig. C1 as a function of $r = |z_0 + z|$. The term T_o is plotted relative to the period of a particle circulating around an isolated vortex T_r [$T_r = 2\pi r/u_r$, and from Eq. (3) $u_r = \Gamma/2\pi r$, such that $T_r = (2\pi r)^2/\Gamma$]. In both cases, $z_0 = l/2$ and $l/5$, when $r/l \ll 1$, $T_o \to T_r$, so that $T_o \sim (2\pi r)^2/\Gamma$ is a reasonable approximation. In the $z_0 = l/2$ case, when the $r/l \ll 1$ condition is not satisfied, $T_o > T_r$, for example, when $r = 15l/32 \sim 0.47l$, $T_o/T_r = 1.339$, so that $T_o = 1.339(\pi 15/16)^2 l^2/\Gamma$. For the $z_0 = l/5$ case, it can be seen that $T_o < T_r$, when $z < -l/5$ and $T_o > T_r$, when $z > -l/5$. In particular, when $z = -3l/10$ ($r = l/10$) $T_o/T_r = 0.793$ and when $z = -l/10$ ($r = l/10$) $T_o/T_r = 1.96$, thus for the special case of the trapped particles in Figs. 10f and 10j, an effective T_o/T_r can be determined by the mean of these two values so that $T_o \sim 1.37T_r = 1.37(\pi/5)^2 l^2/\Gamma$.

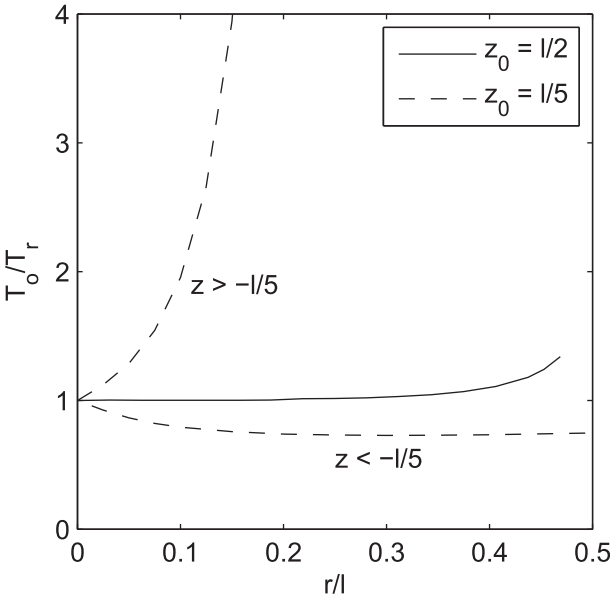

FIG. C1. Orbital period T_o for particle placed at $(l/2, z)$, $-l \le z \le 0$, relative to the period of for an isolated vortex vs r/l for a vortex fixed in place at $(l/2, -z_0)$, where $r = |z_0 + z|$ in a finite-depth square Lc cell.

APPENDIX D

Vortex Streamfunction in the Finite-Depth Case

As before the vortex streamfunction is $\psi(\zeta_0^*) = \mathrm{Im}[\Omega(\zeta_0^*)]$, where $\Omega(\zeta_0^*)$ is given by Eq. (13) evaluated at ζ_0^*, with the self-potential removed, which as $N \to \infty$ can be expressed as

$$\Omega(\zeta_0^*) = i\frac{\Gamma}{2\pi}\log\left(\frac{-i\sin\xi_0 \sinh\chi_0}{\sin\zeta_0^*}\right) + i\frac{\Gamma}{2\pi}\sum_{n=1}^{\infty}\log\left[\frac{\sin(\xi_0 - inp\pi)\sinh(\chi_0 + np\pi)}{\sinh np\pi \sin(\zeta_0^* - inp\pi)}\right] + \log\left[-\frac{\sin(\xi_0 + inp\pi)\sinh(\chi_0 - np\pi)}{\sinh np\pi \sin(\zeta_0^* + inp\pi)}\right]. \qquad \text{(D1)}$$

For the first term the argument can be expressed simply as $(\cot\xi_0 + i\coth\chi_0)^{-1}$. The first and second arguments in the second term for each n can be expressed as $(\pm\coth pn\pi - i\cot\xi_0)/[\coth(\chi_0 \pm pn\pi) - i\cot\xi_0]$. Equation (D1) can then be written

$$\Omega(\zeta_0^*) = -i\frac{\Gamma}{2\pi}\log(\cot\xi_0 + i\coth\chi_0) - i\frac{\Gamma}{2\pi}\sum_{n=1}^{\infty}\log\left(-\frac{P_n + iQ_n}{R_{1n}R_{2n}}\right), \qquad \text{(D2)}$$

where $P_n = -(1 - \coth^2 np\pi \coth^2\chi_0) - R_{2n}\cot^2\xi_0$, $Q_n = 2(1 - \coth^2 np\pi)\cot\xi_0 \coth\chi_0$, $R_{1n} = (\coth^2 np\pi + \cot^2\xi_0)$, and $R_{2n} = (\coth^2 np\pi - \coth^2\chi_0)$. The vortex streamfunction $\psi(\zeta_0^*) = \mathrm{Im}[\Omega(\zeta_0^*)]$ is

$$\psi(\zeta_0^*) = -\frac{\Gamma}{4\pi}\log\left[(\cot^2\xi_0 + \coth^2\chi_0)\prod_{n=1}^{\infty}\frac{P_n^2 + Q_n^2}{R_{1n}^2 R_{2n}^2}\right]. \qquad \text{(D3)}$$

As $n \to \infty$, $\coth^2 np\pi = 1$, such that for large n, $P_n = -R_{1n}R_{2n}$, $Q_n = 0$, and therefore $(P_n^2 + Q_n^2)/R_{1n}^2 R_{2n}^2 = 1$, resulting in a negligible contribution to $\psi(\zeta_0^*)$. Since $\coth^2 2\pi = 1.000\,014$, $\psi(\zeta_0^*)$ can be expressed approximately by truncating the product at $n = 2$, provided that $p \ge 1/2$.

REFERENCES

Batchelor, G. K., 2000: *An Introduction to Fluid Dynamics*. Cambridge University Press, 615 pp.

Belcher, S. E., and Coauthors, 2012: A global perspective on Langmuir turbulence in the ocean surface boundary layer. *Geophys. Res. Lett.*, **39**, L18605, doi:10.1029/2012GL052932.

Bhaskaran, R., and S. Leibovich, 2002: Eulerian and Lagrangian Langmuir circulation patterns. *Phys. Fluids*, **14**, 2557–2571, doi:10.1063/1.1471876.

Clever, R. M., and F. H. Busse, 1992: Three-dimensional convection in a horizontal fluid layer subjected to a constant shear. *J. Fluid Mech.*, **234**, 511–527, doi:10.1017/S0022112092000892.

Craik, A. D. D., and S. Leibovich, 1976: A rational model for Langmuir circulations. *J. Fluid Mech.*, **73**, 401–426, doi:10.1017/S0022112076001420.

Crow, S. C., 1970: Stability theory for a pair of trailing vortices. *AIAA J.*, **8**, 2172–2179, doi:10.2514/3.6083.

Csanady, G. T., 1994: Vortex pair model of Langmuir circulation. *J. Mar. Res.*, **52**, 559–581, doi:10.1357/0022240943076984.

Deloncle, A., P. Billant, and J.-M. Chomaz, 2011: Three-dimensional stability of vortex arrays in a stratified and rotating fluid. *J. Fluid Mech.*, **678**, 482–510, doi:10.1017/jfm.2011.121.

Faller, A. J., 1971: Oceanic turbulence and the Langmuir circulations. *Annu. Rev. Ecol. Syst.*, **2**, 201–236, doi:10.1146/annurev.es.02.110171.001221.

——, and S. J. Auer, 1988: The roles of Langmuir circulations in the dispersion of surface tracers. *J. Phys. Oceanogr.*, **18**, 1108–1123, doi:10.1175/1520-0485(1988)018<1108:TROLCI>2.0.CO;2.

Farmer, D., and M. Li, 1995: Patterns of bubble clouds organized by Langmuir circulation. *J. Phys. Oceanogr.*, **25**, 1426–1440, doi:10.1175/1520-0485(1995)025<1426:POBCOB>2.0.CO;2.

——, S. Vagel, and M. Li, 2001: Bubble and temperature fields in Langmuir circulation. *Fluid Mechanics and the Environment: Dynamical Approaches*, J. Lumley, Ed., Springer, 91–105.

Gargett, A. E., and J. R. Wells, 2007: Langmuir turbulence in shallow water. Part 1. Observations. *J. Fluid Mech.*, **576**, 27–61, doi:10.1017/S0022112006004575.

Gemmrich, J. R., and D. M. Farmer, 1999: Near-surface turbulence and thermal structure in a wind-driven sea. *J. Phys. Oceanogr.*, **29**, 480–499, doi:10.1175/1520-0485(1999)029<0480:NSTATS>2.0.CO;2.

Kenney, B. C., 1977: An experimental investigation of the fluctuating currents responsible for the generation of windrows. Ph.D. thesis, University of Waterloo, 163 pp.

Kukulka, T., A. J. Plueddemann, J. H. Trowbridge, and P. P. Sullivan, 2010: Rapid mixed layer deepening by the combination of Langmuir and shear instabilities: A case study. *J. Phys. Oceanogr.*, **40**, 2381–2400, doi:10.1175/2010JPO4403.1.

Lamb, H., 1932: *Hydrodynamics*. Cambridge University Press, 738 pp.

Langmuir, I., 1938: Surface motion of water induced by wind. *Science*, **87**, 119–123, doi:10.1126/science.87.2250.119.

Leibovich, S., 1983: The form and dynamics of Langmuir circulations. *Annu. Rev. Fluid Mech.*, **15**, 391–427, doi:10.1146/annurev.fl.15.010183.002135.

Li, M., and C. Garrett, 1993: Cell merging and jet/downwelling ratio in Langmuir circulation. *J. Mar. Res.*, **51**, 737–769, doi:10.1357/0022240933223945.

——, ——, and E. Skyllingstad, 2005: A regime diagram for classifying turbulent large eddies in the upper ocean. *Deep-Sea Res. I*, **52**, 259–278, doi:10.1016/j.dsr.2004.09.004.

Longuet-Higgins, M. S., 1981: Oscillatory flow over steep sand ripples. *J. Fluid Mech.*, **107**, 1–36, doi:10.1017/S0022112081001651.

Malarkey, J., and A. G. Davies, 2002: Discrete vortex modelling of oscillatory flow over ripples. *Appl. Ocean Res.*, **24**, 127–145, doi:10.1016/S0141-1187(02)00035-4.

McWilliams, J. C., P. P. Sullivan, and C.-H. Moeng, 1997: Langmuir turbulence in the ocean. *J. Fluid Mech.*, **334**, 1–30, doi:10.1017/S0022112096004375.

——, E. Huckle, J.-H. Liang, and P. P. Sullivan, 2012: The wavy Ekman layer: Langmuir circulations, breaking waves, and Reynolds stress. *J. Phys. Oceanogr.*, **42**, 1793–1816, doi:10.1175/JPO-D-12-07.1.

Milne-Thomson, L. M., 1962: *Theoretical Hydrodynamics*. Macmillan, 660 pp.

Noh, Y., H. S. Min, and S. Raasch, 2004: Large eddy simulation of the upper mixed layer: The effects of wave breaking and Langmuir circulation. *J. Phys. Oceanogr.*, **34**, 720–735, doi:10.1175/1520-0485(2004)034<0720:LESOTO>2.0.CO;2.

——, G. Goh, and S. Raasch, 2011: Influence of Langmuir circulation on the deepening of the wind-mixed layer. *J. Phys. Oceanogr.*, **41**, 472–484, doi:10.1175/2010JPO4494.1.

Pizzo, N. E., and W. K. Melville, 2013: Vortex generation by deep-water breaking waves. *J. Fluid Mech.*, **734**, 198–218, doi:10.1017/jfm.2013.453.

Pollard, R. T., 1977: Observations and theories of Langmuir circulations and their role in near surface mixing. *A Voyage of Discovery—George Deacon 70th Anniversary Volume*, M. Angel, Ed., Pergamon Press, 235–251.

Robinson, A. C., and P. G. Saffman, 1982: Three-dimensional stability of vortex arrays. *J. Fluid Mech.*, **125**, 411–427, doi:10.1017/S0022112082003413.

Rosenhead, L., 1929: The Kármán street of vortices in a channel of finite breadth. *Philos. Trans. Roy. Soc. London*, **A228**, 659–669, doi:10.1098/rsta.1929.0007.

Skyllingstad, E. D., and D. W. Denbo, 1995: An ocean large-eddy simulation of Langmuir circulations and convection in the surface mixed layer. *J. Geophys. Res.*, **100**, 8501–8522, doi:10.1029/94JC03202.

——, W. D. Smyth, J. N. Moum, and H. Wijesekera, 1999: Upper-ocean turbulence during a westerly wind burst: A comparison of large-eddy simulation results and microstructure measurements. *J. Phys. Oceanogr.*, **29**, 5–28, doi:10.1175/1520-0485(1999)029<0005:UOTDAW>2.0.CO;2.

Smith, J. A., 1998: Evolution of Langmuir circulation during a storm. *J. Geophys. Res.*, **103**, 12 649–12 668, doi:10.1029/97JC03611.

Stommel, H., 1949: Trajectories of small bodies sinking slowly through convection cells. *J. Mar. Res.*, **8**, 24–29.

——, 1951: Streaks on natural water surfaces. *Weather*, **6**, 72–74, doi:10.1002/j.1477-8696.1951.tb01309.x.

Sullivan, P. P., J. C. McWilliams, and W. K. Melville, 2007: Surface gravity wave effects in the oceanic boundary layer: Large-eddy simulation with vortex force and stochastic breakers. *J. Fluid Mech.*, **593**, 405–452, doi:10.1017/S002211200700897X.

Sutherland, P., and W. K. Melville, 2015: Field measurements of surface and near-surface turbulence in the presence of breaking waves. *J. Phys. Oceanogr.*, **45**, 943–965, doi:10.1175/JPO-D-14-0133.1.

Tandon, A., and S. Leibovich, 1995: Simulations of three-dimensional Langmuir circulation in water of constant density. *J. Geophys. Res.*, **100**, 22 613–22 623, doi:10.1029/95JC02487.

Thorpe, S. A., 1992: The break-up of Langmuir circulation and the instability of an array of vortices. *J. Phys. Oceanogr.*, **22**, 350–360, doi:10.1175/1520-0485(1992)022<0350:TBOLCA>2.0.CO;2.

——, 2004: Langmuir circulation. *Annu. Rev. Fluid Mech.*, **36**, 55–79, doi:10.1146/annurev.fluid.36.052203.071431.

——, 2009: Spreading of floating particles by Langmuir circulation. *Mar. Pollut. Bull.*, **58**, 1787–1791, doi:10.1016/j.marpolbul.2009.07.022.

——, and A. J. Hall, 1983: The characteristics of breaking waves, bubble clouds, and near-surface currents observed using side-scan sonar. *Cont. Shelf Res.*, **1**, 353–384, doi:10.1016/0278-4343(83)90003-1.

——, M. S. Cure, A. Graham, and A. J. Hall, 1994: Sonar observations of Langmuir circulation, and estimation of dispersion of floating bodies. *J. Atmos. Oceanic Technol.*, **11**, 1273–1294, doi:10.1175/1520-0426(1994)011<1273:SOOLCA>2.0.CO;2.

von Kármán, T., 1911: Uber den Mechanisms des Widerstands, den ein bewegter Körper in einer Flüssigkeit erfährt. Gottenger Nachrichten, *Math. Phys.*, **k1**, 509–517.

——, 1912: Uber den Mechanisms des Widerstands, den ein bewegter Körper in einer Flüssigkeit erfährt. Gottenger Nachrichten, *Math. Phys.*, **k1**, 547–556.

Weller, R. A., and J. F. Price, 1988: Langmuir circulation within the oceanic mixed layer. *Deep-Sea Res.*, **35**, 711–747, doi:10.1016/0198-0149(88)90027-1.

Zedel, L., and D. Farmer, 1991: Organized structures in subsurface bubble clouds: Langmuir circulation in the upper ocean. *J. Geophys. Res.*, **96**, 8889–8900, doi:10.1029/91JC00189.